Coherence control of directional nonlinear photocurrent in spatially symmetric systems

Yongliang Shi [1] and Jian Zhou [2,*]

[1]*Center for Spintronics and Quantum Systems, State Key Laboratory for Mechanical Behavior of Materials,*
Xi'an Jiaotong University, Xi'an 710049, China
[2]*Center for Alloy Innovation and Design, State Key Laboratory for Mechanical Behavior of Materials,*
Xi'an Jiaotong University, Xi'an 710049, China

The interplay between crystal symmetry and its optical responses is at the heart of tremendous recent advances in light-matter interactions and applications. Nonlinear optical processes that produce electric currents, for example the bulk photovoltaic (BPV) effect, require inversion-symmetry-broken materials, such as ferroelectrics. In this work, we demonstrate that such BPV current could be generated in centrosymmetric materials with excitation of out-of-equilibrium coherent phonons. This is very different from the generally studied static or thermally excited states. We show that depending on the coherent phonon phase factor, the photoconductivity contains a static zero-frequency component, as well as THz frequency components. This indicates that a unidirectional current may emerge under synergistic effects of atomic vibration and light irradiation. We also generalize the conventional injection charge current into angular momentum (spin and orbital) degrees of freedom, and demonstrate spin and orbital BPV photoconductivities under coherent phonons. Our findings open the pathway to exploring the exotic phonon-photon-electron coherent interactions in quantum materials.

I. INTRODUCTION

Light-matter interaction is one of the key routes to manipulating electrons and converting light energy into electrical energy. Conventional light energy harvesting and conversion into electric current rely on semiconductor heterostructures (such as *p-n* junctions), in which electrons and holes can be spatially separated under a built-in electric field. This requirement can be eliminated when one uses a single crystal with noncentrosymmetric structure ($\mathcal{P}$-broken), and light illumination could generate direct electric current, known as the bulk photovoltaic (BPV) effect [1,2]. The inversion asymmetry yields anharmonic electric field potential, leading to a collective motion of electrons under light irradiation (when photon energy $\hbar\omega$ is typically larger than semiconductor band gap E_g). Here, $\mathcal{P}$-broken is an acknowledged condition to generate bias-free photocurrent.

The requirement of $\mathcal{P}$-broken limits the candidate material set to produce photocurrents (including shift current and injection current, depending on the crystal symmetry and light polarization). Both shift and injection current processes have been widely observed in various materials, including ferroelectrics, quantum wells, organic crystals, and two-dimensional (2D) interfaces. One has to note that most previous works focus on ferroelectrics in their static or thermally equilibrium state, which are inherently $\mathcal{P}$-broken [3,4]. In this work, we suggest that the injection photocurrent can be triggered in spatially symmetric materials with coherent phonon oscillation excited under a THz pulse irradiation.

Note that coherent phonon vibrations have been proved to induce structural and electronic phase transition in several systems, owing to the fast development of femtosecond laser technology [5,6]. We perform first-principles density functional theory calculations (see Supplemental Note 1 in the Supplemental Material, SM [7]) [8–22] and use a spatially centrosymmetric system, the 2D phosphorene (α-P) monolayer [23], to illustrate our theory. The 2D materials are advantageous for their easy optical access and manipulation [16,24,25], owing to their ultrathin nature. In addition, the direct optical absorption is much reduced in 2D thin films; hence the hot carrier mobility drift current can be marginal, yielding better experimental observations. We show that the zone-center ($q = 0$) infrared (IR) active phonon can be excited under a THz laser pulse with intermediate fluence, which brings coherent odd-parity mode oscillations. Under such dynamic state, circularly polarized light (CPL) irradiation could produce a nonzero unidirectional propagating current, according to the injection photocurrent mechanism. One has to note that even though the average displacements of such coherent phonon vibration is zero, which corresponds to the static centrosymmetric geometry, the photon-irradiation-induced injection current does not vanish and could contain a static current component. Such counterintuitive phenomenon arises due to the injection current microscopic mechanism, which reflects the velocity mismatch between the valence and conduction bands. The direction of such photocurrent can be determined by the phonon vibration phase when the CPL irradiates, and thus a coherent control [26] of electric charge current can be realized. Furthermore, we propose that under linearly polarized light (LPL) irradiation, one could generate angular momentum (AM) related photocurrent (both

*jianzhou@xjtu.edu.cn

spin BPV current and orbital BPV current), which has similar injection current nature. This generalizes the photoinduced nanoelectronics into spin and orbital AM degrees of freedom, which carries magnetic moment information. Therefore, dynamic but nonzero photocurrent with tunable transport direction (rather than a pure THz alternating current which averages to be zero over time) and carrying charge, spin, and orbital information can be produced via a synergistic cooperation of coherent phonon and second-order nonlinear injection BPV approaches. Such mechanism can be extended to other spatially (vertical mirror) symmetric materials, such as the H-MoS$_2$ monolayer [27].

According to nonlinear optics theory, once a CPL irradiates onto a nonmagnetic ($\mathcal{T}$-symmetric) material, its helicity phase generates injection current that is proportional to the interband Berry curvature (usually also known as the circular photogalvanic effect [28]). In this process, light excites carriers into velocity-asymmetrical states in the Brillouin zone (BZ) and produces a net charge current [29–33]. The second-order photoconductivity $\sigma(0; \omega, -\omega)$ grows linearly with time, and saturates when the carrier relaxation time τ is met. This is different from shift current which is τ-independent. Hence, we evaluate its rate (see Supplemental Note 2 in the SM [7]),

$$\eta_{bc}^a(\omega) = \frac{d}{dt}\sigma_{bc}^a(0; \omega, -\omega) = -\frac{\pi e^3}{2\hbar^2}\int_{BZ}\frac{d^2\boldsymbol{k}}{(2\pi)^2}$$

$$\times \operatorname{Im}\sum_{l,m} f_{lm}\Delta_{lm}^a [r_{ml}^b, r_{lm}^c]\delta(\omega_{ml} - \omega). \quad (1)$$

Here a, b, c indicate 2D Cartesian indices x and y. $f_{lm} = f_l - f_m$ and $\Delta_{lm}^a = v_{ll}^a - v_{mm}^a$ are the occupation and velocity difference between bands l and m, respectively. The interband transition dipole is $r_{ml}^b = \langle m|r^b|l\rangle$. Note that all explicit $\boldsymbol{k}$ dependencies of quantities are omitted. The commutator $[r_{ml}^b, r_{lm}^c] = r_{ml}^b r_{lm}^c - r_{ml}^c r_{lm}^b = -i\epsilon_{abc}\Omega_{ml}^a$ corresponds to interband Berry curvature. In the current work, we use the Lorentzian function to represent the Dirac δ function, with a broadening factor of 0.02 eV. It phenomenologically incorporates the temperature, disorder, and scattering effects. Note that a larger broadening factor does not affect the main conclusion in this work. The total current density emerges according to $j_{\text{inj}}^a = 2\sigma_{bc}^a(0; \omega, -\omega)E_b(\omega)E_c(-\omega)$, where E_i is the optical electric field component. The actual photocurrent depends on the width and depth of light illumination [4], and one has to note that other photocurrent mechanisms may also exist. According to Eq. (1), the different velocities at the valence and conduction bands could produce net injection photocurrent. For the 2D BZ integration which lacks the out-of-plane k_z component, the calculated η (and σ) includes a surplus length unit (nm or Å) compared with that in conventional 3D crystals. In order to eliminate such difference and adopt the 3D unit systems, we rescale them by utilizing an effective thickness of the system, $\eta^{\text{eff}} = \eta^{\text{2D}}/d$. Here d refers to the monolayer effective thickness (taken to be 6 Å in the current work), and the superscripts "2D" and "eff" indicate 2D values and the rescaled effective 3D results. This is similar as linear response theory calculated dielectric functions, based on a parallel capacitor model, and has been widely adopted previously [24,34–36]. In this work, we report the rescaled values. Note that when deducing actual current, one has to
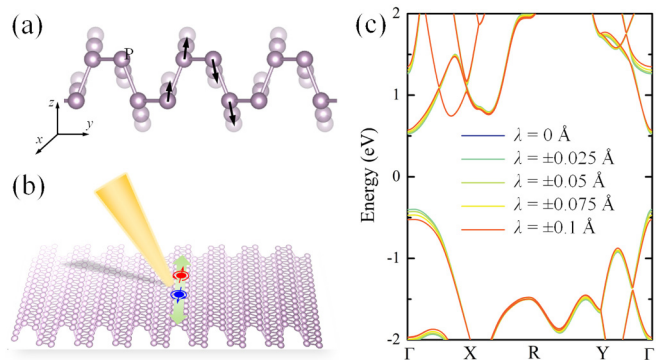
FIG. 1. (a) THz optics irradiation inducing coherent IR-active phonon vibration in α-P monolayer. The mode displacement amplitude is enlarged for clarity reasons. (b) Nonlinear injection photocurrent moves along the x (zigzag) direction. (c) Quasistatic band dispersion variation under displacement λ.

multiply such effective thickness [37]. Thus, this choice of effective thickness d does not affect any measurable physical quantities, which is akin to the "gauge" choice in a process that is gauge invariant.

II. RESULTS

A. Coherent vibration of α-P monolayer and injection current rate under CPL

According to symmetry arguments, we limit our discussion to the zone-centered phonon modes (unit cell wavelength coherent oscillation), which can be effectively excited via THz optics (Fig. S1 in the SM [7]). In the α-P monolayer, the only mode is B_{1u} (at 4.2 THz = 140 cm^{-1}), which breaks $\mathcal{P}$ and introduces dynamic in-plane polarization [$P_y(t) \neq 0$]. This mode mainly displaces P atoms out-of-plane, as shown in Fig. 1(a). We find that the anharmonicity of B_{1u} is very weak, suggesting its small damping effect and long lifetime during operation. Now we displace atoms according to their phonon eigenvectors, and use λ to measure the total displacements of all four atoms in a unit cell. When $\lambda = \pm 0.1$ Å, the energy gain is 10 meV per atom. This corresponds to a THz laser pulse with pump fluence of 0.25 mJ/cm^2 centered at 4.2 THz. The positive and negative λ correspond to spatially opposite images, i.e., atomic coordinates $\mathbf{x}_i^\lambda = -\mathbf{x}_i^{-\lambda}$ for each atom i. Hence, they show the same electronic band structure [Fig. 1(c)].

The coherent B_{1u} reduces the space group from static $Pmna$ to $Pmn2_1$ dynamically, which breaks the $\mathcal{M}_y$ mirror symmetry but preserves $\mathcal{M}_x$. According to our symmetry analysis (see Supplemental Note 3 in the SM [7]), dynamic injection current then emerges under CPL and would flow along the x direction. Here we will only discuss η_{xy}^x because $\eta_{yx}^x = -\eta_{xy}^x$. Since the ionic vibration period is on a few hundreds of picoseconds, one can safely assume that electrons effectively experience a quasistatic potential field under different λ. We also calculate the band edge dephasing time, which is found to be on the order of femtoseconds, and increases as temperature reduces (see Fig. S2 in the SM [7]). This is consistent with the previous work [38], and is sufficiently long
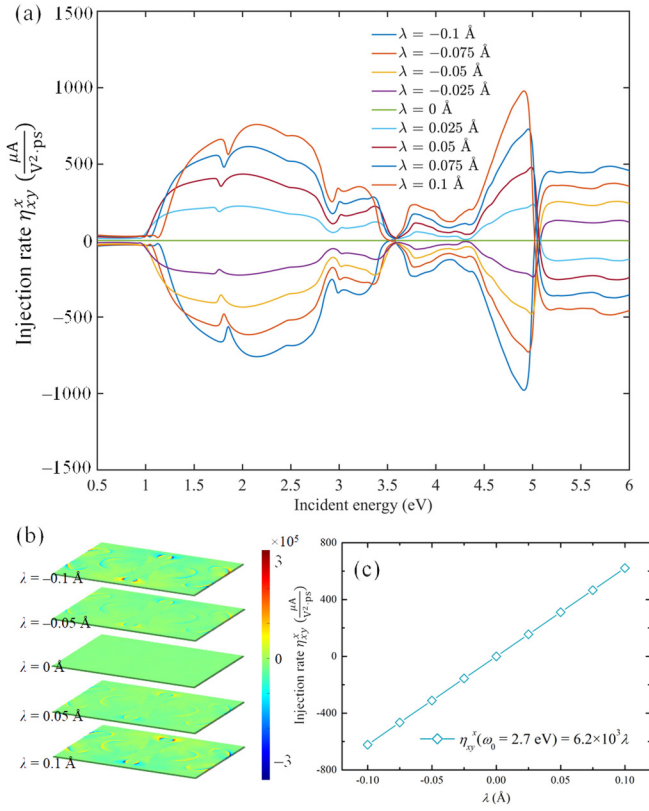
FIG. 2. (a) Injection photocurrent rate η_{xy}^x of α-P in various λ states. (b) $\boldsymbol{k}$-resolved contribution of injection photocurrent rate at $\omega_0 = 2.7$ eV. (c) Linear fitting of $\eta_{xy}^x(\omega_0)$ with λ.

for nonlinear optical process (absorbing and releasing photons during the two-photon-one-electron process). Figure 2(a) shows the injection current rate as a function of different displacement. One clearly sees that positive and negative λ give opposite photoconductivity rates [$\eta_{xy}^x(\lambda) = -\eta_{xy}^x(-\lambda)$], even though their band dispersions are the same. We also plot the $\boldsymbol{k}$-resolved integrand of Eq. (1) at a selected optical incident energy $\omega_0 = 2.7$ eV, which shows large contribution near the Γ-Y path [Fig. 2(b)]. This distribution is a bit different from the joint density of states (see Fig. S3 in the SM [7]), suggesting an anisotropic interband transition contribution $\langle m|\boldsymbol{r}|n\rangle$ at different $\boldsymbol{k}$. We then fit $\eta_{xy}^x(\omega_0)$ with respect to λ by linear regression $\eta_{xy}^x(\omega_0) = C_1\lambda + o(\lambda^2)$ [Fig. 2(c)], which gives $C_1 = 6.2 \times 10^3 \frac{\mu\text{A}}{\text{V}^2\,\text{A}\,\text{ps}}$.

B. Angular momentum current under LPL irradiation

Photocurrent generated by CPL also includes the LPL shift current feature, while LPL irradiation does not suffer such a problem [39]. Hence, next we consider the LPL-induced injection current. For time-reversal symmetry systems, we have recently demonstrated that LPL could generate AM photocurrents, showing an injection current feature [36,40]. Photoinduced AM currents include both spin and orbital currents. They roughly indicate that electrons carrying opposite spin and orbital moments are flowing oppositely. Note that orbital angular momentum is a largely overlooked degree of freedom that has attracted increasing attention recently [41].

We evaluate the spin (and orbital) photocurrent conductivity rate [36,42–44],

$$\eta_{bc}^{a;\hat{O}_z}(\omega) = \frac{d}{dt}\sigma_{bc}^{a;\hat{O}_z}(0;\omega,-\omega) = -\frac{\pi e^3}{2\hbar^2}\int_{\text{BZ}}\frac{d^2\boldsymbol{k}}{(2\pi)^2}$$
$$\times \text{Re}\sum_{l,m}f_{lm}j_{lm}^{a;\hat{O}_z}\{r_{ml}^b, r_{lm}^c\}\delta(\omega_{ml}-\omega). \quad (2)$$

Here $j_{lm}^{a;\hat{O}_z}$ denotes the difference of angular momentum current for bands l and m, and $j^{a;\hat{O}_z} = \{v_a, \hat{O}_z\}/2e$, ($\hat{O} = \hat{S}, \hat{L}$) [21,45]. The $\{r_{ml}^b, r_{lm}^c\}$ refers to anticommutation between r_{ml}^b and r_{lm}^c. Here we focus on the spin-z and orbital-z components, since they are unidirectionally pointing along the out-of-plane direction in most $\boldsymbol{k}$ points (singly degenerate) [36,46]. This is because $\boldsymbol{S}$ and $\boldsymbol{L}$ are pseudovectors and the $Pmn2_1$ contains a glide mirror operation $\{\mathcal{M}_z|\frac{1}{2}\frac{1}{2}0\}$. Under IR-active vibration, the α-P monolayer is symmetrically the same as group-IV monochalcogenide monolayers, which have been demonstrated to possess anisotropic spin and orbital photocurrents [36,47].

Figure 3 shows our calculated nonlinear spin and orbital photocurrent rates under y-LPL for different λ. The angular momentum distribution and x-LPL responses are plotted in Figs. S4 and S5 in the SM [7]. Similarly to the η_{xy}^x case, the static $\mathcal{P}$-symmetric system has the constraint that $\eta_{yy}^{x;S_z}(\lambda = 0) = 0$ and $\eta_{yy}^{x;L_z}(\lambda = 0) = 0$. Positive and negative λ give opposite values for the AM photocurrent rates. One has to note that under LPL, there is no shift current along x, due to the presence of $\mathcal{M}_x$. Thus, no charge current is mixed in this case, indicating pure spin and orbital currents. We observe that the orbital photocurrent has larger values than the spin photocurrent, owing to small spin-orbit coupling in P. This is in contrast with the common picture that orbital moments are usually quenched in magnetic systems under strong and isotropic crystal field effects, where magnetism is mainly from the spin degree of freedom. We also fit these photocurrent rates at $\omega_0 = 2.7$ eV by odd power polynomial functions using λ, $\eta_{yy}^{x;S_z}(\omega_0) = C_1^S\lambda + C_3^S\lambda^3 + o(\lambda^4)$ and $\eta_{yy}^{x;L_z}(\omega_0) = C_1^L\lambda + C_3^L\lambda^3 + o(\lambda^5)$. Our results are $C_1^S = -10.8$, $C_3^S = -2.3 \times 10^3$, $C_1^L = -4.6 \times 10^3$, and $C_3^L = -6.7 \times 10^4$. The units of $C_1^{S,L}$ and $C_3^{S,L}$ are $\frac{\mu\text{A}}{\text{V}^2\,\text{A}\,\text{ps}}\frac{\hbar}{2e}$ and $\frac{\mu\text{A}}{\text{V}^2\,\text{A}^3\,\text{ps}}\frac{\hbar}{2e}$, respectively. Both of them show strong nonlinear λ^3 relationships due to the interplay of band gap and wave function variations under B_{1u}.

C. Time-dependent injection charge, spin, and orbital currents

We now integrate η in time to explore these second-order photoconductivities under coherent B_{1u} oscillation,

$$\frac{d\sigma_{\text{inj}}(t)}{dt} = \eta(\omega_0, \lambda(t)), \quad (3)$$

where $\lambda(t) = \lambda_0 \sin(2\pi\omega_{\text{IR}}t + \phi)$ is the B_{1u} mode vibration equation of motion with amplitude of $\lambda_0 = 0.1$ Å and frequency $\omega_{\text{IR}} = 4.2$ THz. $\phi \in (-\pi, \pi]$ is the vibration phase at the initial state ($t = 0$). The initial condition is $\sigma_{\text{inj}}(t = 0) = 0$. Note that as discussed previously, the injection current saturates at its carrier relaxation lifetime τ [40,48], which is finite and depends on the quality of the sample, temperature, electron-electron scattering, and electron-phonon coupling.
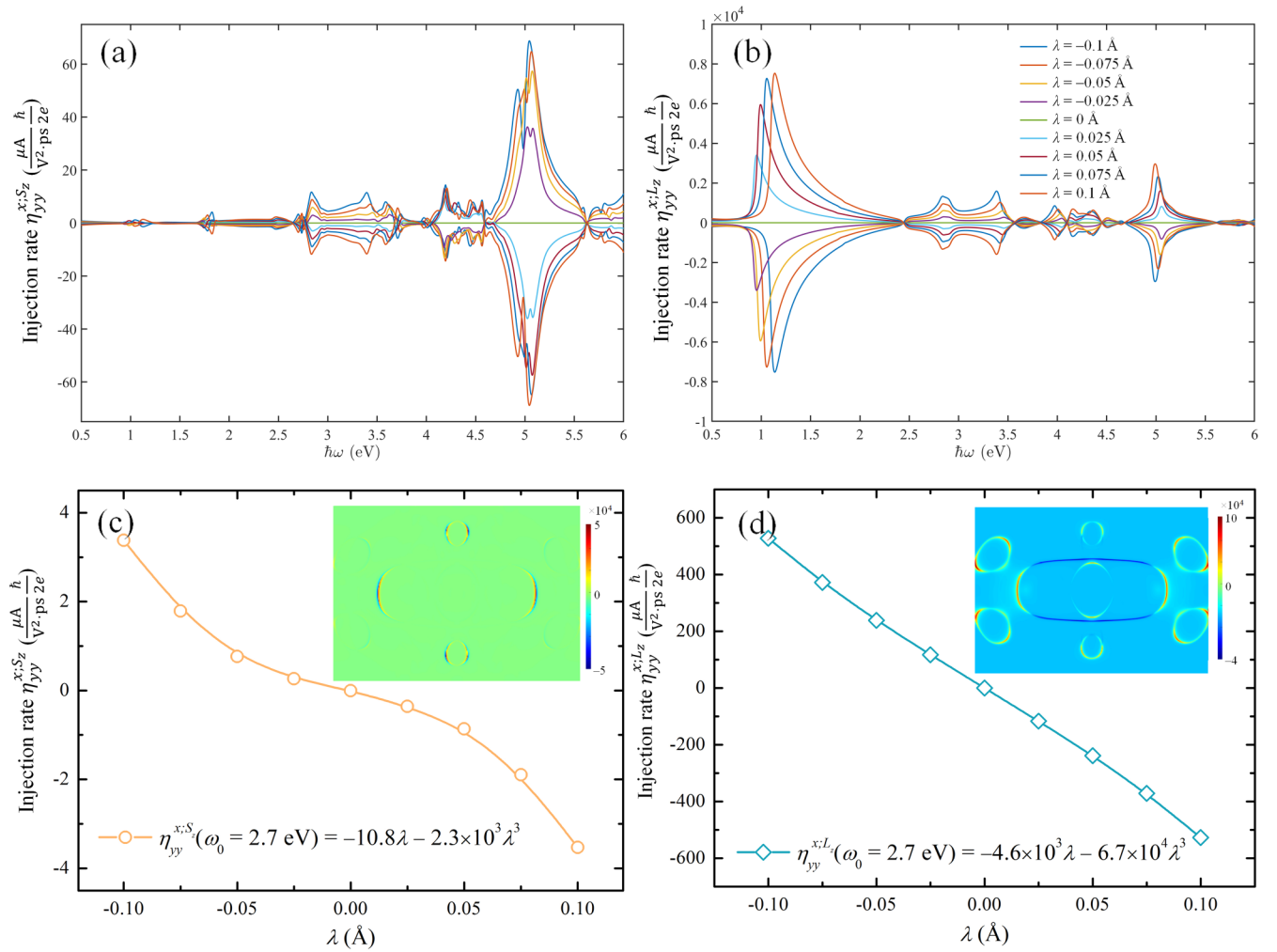
FIG. 3. (a) Spin and (b) orbital photocurrent rate under different λ. Panels (c) and (d) show their λ dependence at $\omega_0 = 2.7$ eV. Insets show the $\mathbf{k}$-resolved contributions at $\lambda = -0.1$ Å.

This is different from the above-mentioned dephasing time, which measures the correlation between wave function phases in the valence and conduction bands and is much shorter. The carrier relaxation lifetime is determined by carrier mean free path and velocity, and can survive a much longer time. Here, we assume that such τ is on the order of (sub)picoseconds and is longer than the phonon vibration cycle, which can be realized experimentally [49,50]. The phonon vibration lifetime is usually much longer as well [51], as the anharmonicity (such as three-phonon interactions) is marginal in the current case.

As shown in Figs. 4(a)–4(c), the photocurrent oscillates around an average value, which is determined by ϕ. In the coherent vibration case, this ϕ is the same in different unit cells. When $\phi = \pm\pi/2$, one always obtains an oscillating (charge, spin, and orbital) current. The time average of such current is zero, indicating a pure alternating current (with propagating directions opposite for $\phi = \pi/2$ and $-\pi/2$). When we perform Fourier transformation of such currents [dashed curves in Figs. 4(d)–4(f)], it shows a sharp peak at $\omega_{\mathrm{IR}} = 4.2$ THz. For the spin and orbital photocurrents, additional peaks at $3\omega_{\mathrm{IR}} = 12.6$ THz can be seen, consistent with the λ^3 dependence of $\eta_{yy}^{x;O_z}(\omega_0)$ in these cases. Depending on the incident photon energy, such nonlinearity may be tuned. Remarkably,

when $\phi = 0$ and $\phi = \pi$, one can see that in addition to the oscillatory nature, they also contain large static current features with 0 THz contributions. This indicates that one could observe a *unidirectional* injection photocurrent, the magnitude of which wiggles but it always flows toward one direction. Depending on the sign of C (and C^S, C^L), the photocurrent can be positive or negative. The $\phi = 0$ and $\phi = \pi$ give opposite propagating currents.

We would like to emphasize that Eq. (3) is a simplified model which omits the damping effect and assumes that the carrier relaxation time is sufficiently long ($\tau \to \infty$). In reality, such relaxation time is finite, even in perfect crystals. The scattering between current and crystal, such as phonons, would reduce its lifetime. Hence, we assume a uniform damping effect, by introducing a finite relaxation time τ and the injection current conductivity can be obtained via

$$\frac{d\sigma_{\mathrm{inj}}(t)}{dt} = \eta(\omega_0, \lambda(t)) - \frac{\sigma_{\mathrm{inj}}(t)}{\tau}. \tag{4}$$

We take the CPL-induced injection charge current as an example, and evaluate the $\phi = 0$ and π cases under different τ. The results are plotted in Fig. S6 in the SM [7]. One observes that finite τ would gradually suppress the static current
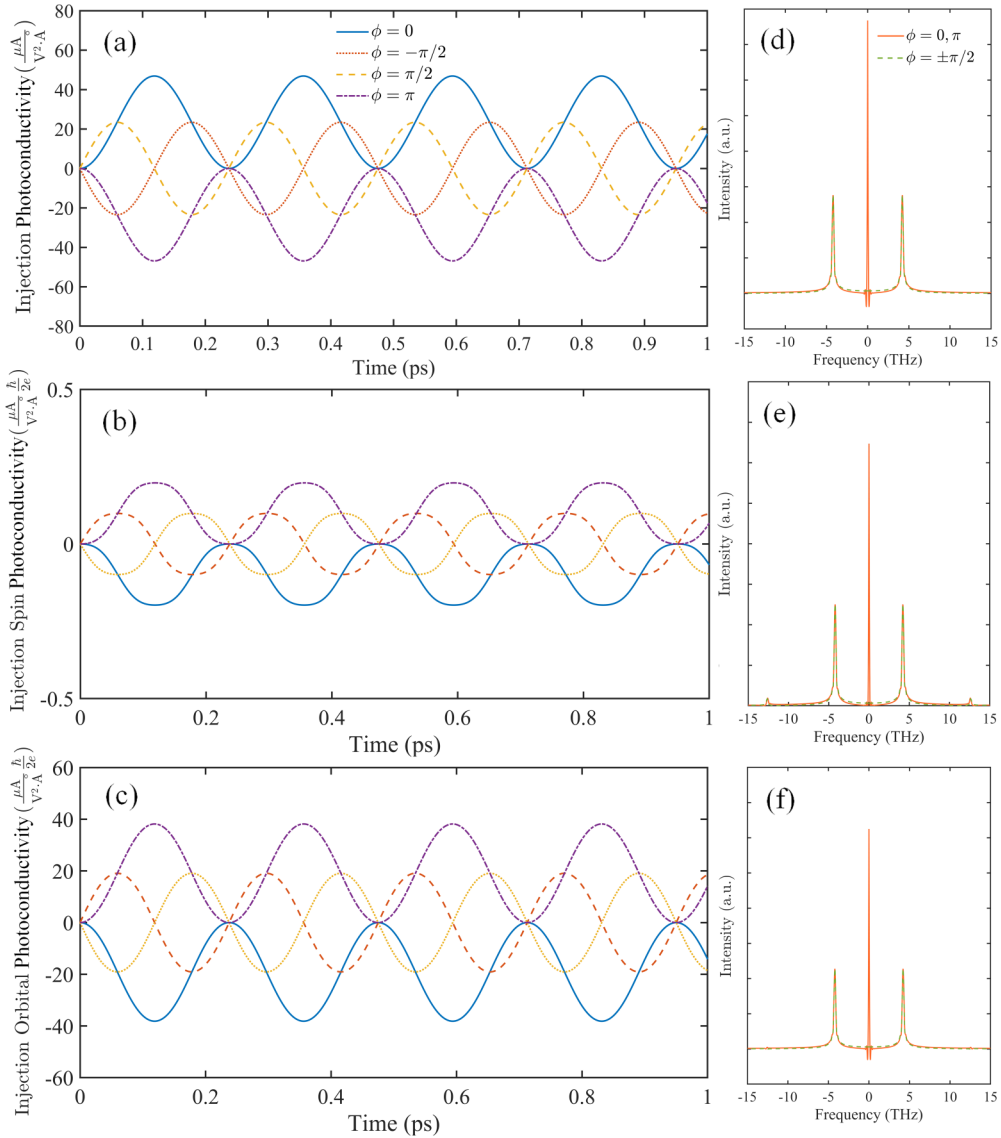
FIG. 4. Time evolution of (a) injection photoconductivity under CPL, (b) spin and (c) orbital photoconductivity under LPL. The current propagation strongly depends on phase ϕ. In (d)–(f) we show frequency distributions of (a)–(c) photocurrents by Fourier transformations. Incident photon energy of $\omega_0 = 2.7$ eV is used.

component. But the THz oscillating current still survives and its amplitude is maintained. This is due to the assumption that phonon lifetime is sufficiently long.

D. Transition metal dichalcogenide monolayer case

So far we have demonstrated that coherent IR-active oscillation could induce finite injection current in a static $\mathcal{P}$-symmetric system, the α-P monolayer. In order to show that it is a universal effect, we now briefly discuss such oscillating injection current in another well-studied monolayer, transition metal dichalcogenide MoTe$_2$ [52]. This system does not possess $\mathcal{P}$ at its static structure, but it includes a vertical mirror plane $\mathcal{M}_x$ [inset of Fig. 5(a)]. It symmetrically forbids CPL injection current and LPL AM photocurrent along y. In the unit cell periodic coherent vibrations, there is a doubly degenerate E' mode (at $\omega'_{IR} = 7.1$ THz) being

IR-active. It contains two vertical vibration eigenvectors, along the x and y directions, respectively. They can be individually excited using linearly polarized THz pulses. Hence, we only focus on the x mode which breaks $\mathcal{M}_x$ dynamically.

We again consider vibrations with λ between -0.1 Å and 0.1 Å. The total energy increases quadratically up to 43 meV per formula unit. The system shows a finite electric polarization along the zigzag direction, P_x, which linearly increases with λ. Then we consider the injection photocurrents. When the ionic system is coherently excited (E'_x), the $\mathcal{M}_x$ symmetry constraints are lifted. From Fig. 5 we plot their values at a chosen incident photon energy (1.7 eV). Nonlinear λ dependence can be clearly observed in this case, especially for orbital and spin photocurrents. If we integrate the photocurrent rate as in Eqs. (3) and (4), we obtain similar unidirectional injection photocurrents (with 0 THz static current component). The
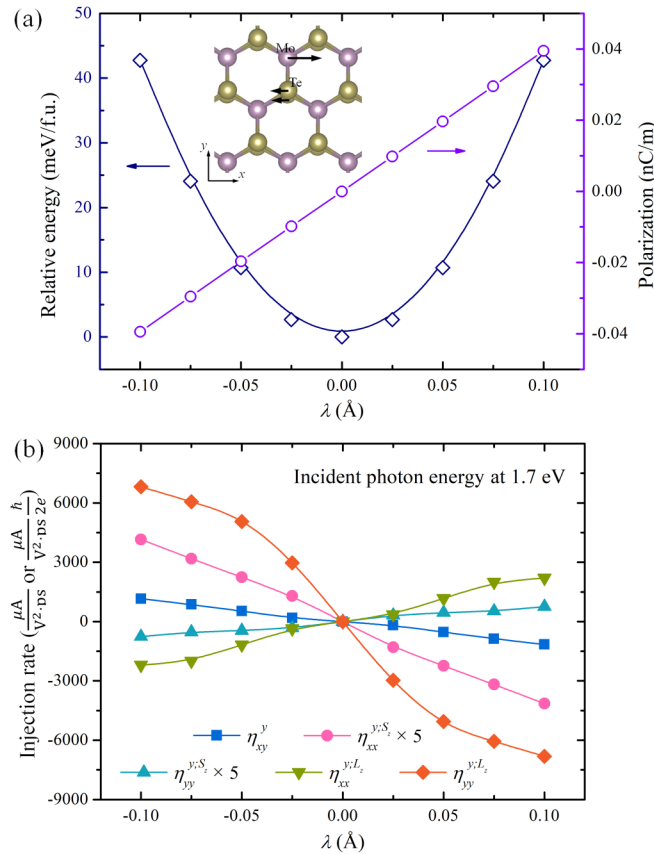
FIG. 5. (a) IR-active mode (along x, zigzag direction) driven variation of total energy and electric polarization (P_x) in MoTe$_2$. Inset shows atomic geometry and vibration mode. Panel (b) shows the variation of injection photocurrent rate under CPL (units of $\frac{\mu A}{V^2\,ps}$) and injection AM photocurrent rate under LPL (units of $\frac{\mu A}{V^2\,ps}\frac{\hbar}{2e}$). All currents propagate along y (armchair).

nonlinear contributions ($3\omega'_{IR}$ and $5\omega'_{IR}$ contributions) can also be obtained (see Fig. S7 in the SM [7]).

III. DISCUSSION

Before concluding, we would like to note that the coherent IR-active vibration at Γ is different from other ionic vibrations or motions, such as thermal excitations, Raman-active modes, or BZ boundary modes. The thermally excited phonons are in the whole BZ with finite q components and random in phase. Hence, they do not possess a definite wavelength. The vibration phase factor ϕ does not have a long-range correlation in different unit cells. The spatial average of phase $\bar{\phi}$ would be zero. Thus, they are different from the collective and coherent motion of ions which has only a $q \sim 0$ component, and the vibration phase is nonzero with long-range correlation. In this regard, the thermally excited phonon vibration will result in behaviors qualitatively similar to those in the static configuration, and both the alternative (at ω_{IR}) and static injection currents would vanish. On the other hand, collective Γ-centered Raman modes and BZ boundary modes usually do not break the spatial symmetry $\mathcal{P}$ or $\mathcal{M}$. Hence, even though they would affect the electronic structure (band dispersion,

etc.) and can change the otherwise existing current values, the spatial symmetry arguments do not break. Then the oscillating effect will be different and may not be as strong as that in the current case. We also want to note that recently Schlipf and Giustino proposed a dynamic Rashba-Dresselhaus (dRD) effect under coherent IR-active phonon oscillations [53], where they showed that the dRD can be observed at a given time t. But in their case the dRD would diminish if time average is performed. In our proposal, on the contrary, one can obtain the static (zero-frequency) photocurrent component, which does not require an ultrafast dynamics observation setup. Of course, the recently developed ultrafast dynamic approaches could provide high-resolution observations of the injection photocurrent [5,6], and would be useful for experimental verification and applications of our prediction.

The α-P and MoTe$_2$ monolayers possess out-of-plane glide and mirror symmetries, respectively. They generally forbid in-plane angular momentum components, since $\boldsymbol{L}$ and $\boldsymbol{S}$ are both axial vectors. However, one has to note that even without spin-orbit coupling, L_z does not commute with the Hamiltonian as it is determined by the crystal field effect. Hence, the orbital angular momentum is generally not a good quantum number. This would yield an additional orbital torque effect [54] in the continuum equation of motion. Actually, a similar problem occurs in spin current (such as quantum spin Hall current) when Rashba spin-orbit coupling is present. Various approaches have been suggested to avoid such problem; for example, one can project L_z onto eigenstate space via $\mathbb{L}_z = \sum_n |\psi_{nk}\rangle\langle\psi_{nk}|L_z|\psi_{nk}\rangle\langle\psi_{nk}|$ [22,45,55], which corresponds to the diagonal terms in density matrix. Then we have $[\mathbb{L}_z, \hat{H}] = 0$. This is consistent with considering the orbital torque effect, and is discussed in Supplemental Note 4 (see the SM [7]). Note that no matter which approaches are used, the symmetry analysis and qualitative results remain the same.

This leads to the definition of angular momentum current, which is also under significant debate [21,45,55–62]. When the out-of-plane spin-z component is conserved, one may define the spin current as $j_{sp} = j_\uparrow - j_\downarrow$, where $\uparrow$ and $\downarrow$ indicate spin-up and spin-down channels, respectively. However, in a general case, the spin current definition is not straightforward. There are several spin current expressions. The current study adopts $j_{sp}^{a;S_z} = \{v_a, S_z\}$, which has been widely used to evaluate the spin Hall effect, spin Seebeck effect, etc. But the spin variation over time is not considered in this form. On the other hand, it has been proposed that a proper definition takes the form of $j_{sp}^{a;S_z} = \frac{d(r_a S_z)}{dt}$ [21], which has been proved to satisfy the continuation equation and Onsager reciprocal relations. The same problem exists in the orbital current situation. The difference between these two approaches can be regarded as the spin (and orbital) torque effect, which yields the same symmetry argument. As discussed in Supplemental Note 4 and Fig. S8 [7], we show that the torque effect is consistent with AM projected onto nondiagonal density matrix contributions.

In this study, we use the quadratic recursive response theory to evaluate the injection current rate, which essentially corresponds to Tr($j^{(0)}\rho^{(2)}$), where $j^{(0)}$ is electric field E independent current operator and $\rho^{(2)}$ is the second-order perturbative density matrix operator. They can be calculated according to Kubo theory. Note that there are other contributions,

such as self-energy and vertex corrections [63], which cannot be simply included in the current density functional theory calculation framework and are not computed here. In addition, the $\text{Tr}(j^{(1)}\rho^{(1)})$ contribution, where $j^{(1)}$ originates from anomalous velocity (interband Berry curvature) and is linearly dependent on electric field E, would vanish in such topologically trivial and insulating systems.

As discussed previously, the bulk photovoltaic effect includes shift current and injection current, which originate from different microscopic mechanisms [4]. Taking electric charge current as an example (similar arguments hold for AM current), the shift current arises from the mismatch of wave function center position in the valence and conduction bands. The shift current conductivity does not depend on carrier relaxation time τ, even though it needs to be finite. On the other hand, injection current originates from the mismatch of velocity operator in the valence and conduction bands. Hence, the injection current *rate* is more fundamental. Most previous studies evaluate the injection current for static configurations via $\sigma_{\text{inj}} = \eta\tau$, where τ is carrier relaxation lifetime, determined by disorder, temperature, impurities, electron-phonon scattering, etc. [31,40,43]. In this study we show that coherent vibration gives a time-dependent rate $\eta(t)$; hence the ultimate injection current can be dynamic, nonzero, and even contains the static component. The shift current, on the contrary, does not possess such property. In realistic experimental setups, the above band gap photon absorption produces hot carriers (electrons and holes), and their drifts contribute to photoconductivities as well (e.g., ballistic current) [64,65]. Note that the ballistic current is proportional to the imaginary part of susceptibility, which indicates the direct band light absorption. We plot the linear response theory (in the framework of the independent particle approximation) calculated electron susceptibility of α-P in Fig. S9 [7]. Note that the carrier relaxation time τ appears in the numerator of the ballistic current response function to account for the distribution function asymmetry, and also in its denominator for phonon corrections to the electron-photon vertex. Hence, its time dependence is more complicated. However, this is not the situation discussed in the current work.

IV. CONCLUSION

In summary, we apply first-principles calculations to show that Γ-centered coherent IR-active phonon oscillation that breaks spatial symmetry could trigger nonlinear injection photocurrent in otherwise silent systems. This photocurrent could be purely alternating or unidirectionally propagating, depending on the phase of the coherent phonon. Our work shows that unlike the widely studied static or thermally equilibrium conditions, the synergistic interplay between the coherent phonon, electron, and photon could lead to intriguing and exotic nonlinear optical responses in ultrafast dynamics. The system setup we propose here may serve as a future THz electromagnetic wave detector for the next generation communication.

ACKNOWLEDGMENTS

---

[1] V. M. Fridkin, Bulk photovoltaic effect in noncentrosymmetric crystals, Cryst. Rep. **46**, 654 (2001).

[2] C. Aversa and J. E. Sipe, Nonlinear optical susceptibilities of semiconductors: Results with a length-gauge analysis, Phys. Rev. B **52**, 14636 (1995).

[3] S.-J. Gong, F. Zheng, and A. M. Rappe, Phonon Influence on Bulk Photovoltaic Effect in the Ferroelectric Semiconductor GeTe, Phys. Rev. Lett. **121**, 017402 (2018).

[4] L. Z. Tan, F. Zheng, S. M. Young, F. Wang, S. Liu, and A. M. Rappe, Shift current bulk photovoltaic effect in polar materials—hybrid and oxide perovskites and beyond, npj Comput. Mater. **2**, 16026 (2016).

[5] L. Luo, D. Cheng, B. Song, L.-L. Wang, C. Vaswani, P. M. Lozano, G. Gu, C. Huang, R. H. J. Kim, Z. Liu, J.-M. Park, Y. Yao, K. Ho, I. E. Perakis, Q. Li, and J. Wang, A light-induced phononic symmetry switch and giant dissipationless topological photocurrent in ZrTe$_5$, Nat. Mater. **20**, 329 (2021).

[6] J. G. Horstmann, B. Böckmann, H. Wit, F. Kurtz, G. Storeck, and C. Ropers, Coherent control of a surface structural phase transition, Nature (London) **583**, 232 (2020).

[7] See Supplemental Material at http://link.aps.org/supplemental/10.1103/PhysRevB.104.155146 for computational details, injection photocurrent mechanisms, symmetry arguments, spin and orbital torque effects, and supplemental figures.

[8] P. Hohenberg and W. Kohn, Inhomogeneous electron gas, Phys. Rev. **136**, B864 (1964).

[9] G. Kresse and J. Furthmüller, Efficient iterative schemes for *ab initio* total-energy calculations using a plane-wave basis set, Phys. Rev. B **54**, 11169 (1996).

[10] J. P. Perdew, K. Burke, and M. Ernzerhof, Generalized Gradient Approximation Made Simple, Phys. Rev. Lett. **77**, 3865 (1996).

[11] P. E. Blöchl, Projector augmented-wave method, Phys. Rev. B **50**, 17953 (1994).

[12] H. J. Monkhorst and J. D. Pack, Special points for Brillouin-zone integrations, Phys. Rev. B **13**, 5188 (1976).

[13] A. Togo and I. Tanaka, First principles phonon calculations in materials science, Scr. Mater. **108**, 1 (2015).

[14] A. A. Mostofi, J. R. Yates, G. Pizzi, Y.-S. Lee, I. Souza, D. Vanderbilt, and N. Marzari, An updated version of Wannier90: A tool for obtaining maximally-localised Wannier functions, Comput. Phys. Commun. **185**, 2309 (2014).

[15] J. Shi, G. Vignale, D. Xiao, and Q. Niu, Quantum Theory of Orbital Magnetization and Its Generalization to Interacting Systems, Phys. Rev. Lett. **99**, 197202 (2007).

[16] H. Xu, J. Zhou, H. Wang, and J. Li, Light-induced static magnetization: Nonlinear Edelstein effect, Phys. Rev. B **103**, 205417 (2021).

[17] M. G. Lopez, D. Vanderbilt, T. Thonhauser, and I. Souza, Wannier-based calculation of the orbital magnetization in crystals, Phys. Rev. B **85**, 014435 (2012).

[18] R. Long and O. V. Prezhdo, Instantaneous generation of charge-separated state on TiO_2 surface sensitized with plasmonic nanoparticles, J. Am. Chem. Soc. **136**, 4343 (2014).

[19] *Principles of Nonlinear Optical Spectroscopy*, edited by S. Mukamel (Oxford University Press, New York, 1995).

[20] Y. Zhang, H. Ishizuka, J. van den Brink, C. Felser, B. Yan, and N. Nagaosa, Photogalvanic effect in Weyl semimetals from first principles, Phys. Rev. B **97**, 241118(R) (2018).

[21] J. Shi, P. Zhang, D. Xiao, and Q. Niu, Proper Definition of Spin Current in Spin-Orbit Coupled Systems, Phys. Rev. Lett. **96**, 076604 (2006).

[22] V. T. Phong, Z. Addison, S. Ahn, H. Min, R. Agarwal, and E. J. Mele, Optically Controlled Orbitronics on a Triangular Lattice, Phys. Rev. Lett. **123**, 236403 (2019).

[23] H. Liu, A. T. Neal, Z. Zhu, Z. Luo, X. Xu, D. Tománek, and P. D. Ye, Phosphorene: An unexplored 2D semiconductor with a high hole mobility, ACS Nano **8**, 4033 (2014).

[24] J. Zhou, H. Xu, Y. Li, R. Jaramillo, and J. Li, Opto-mechanics driven fast martensitic transition in two-dimensional materials, Nano Lett. **18**, 7794 (2018).

[25] H. Guo, W. Chu, O. V. Prezhdo, Q. Zheng, and J. Zhao, Strong modulation of band gap, carrier mobility and lifetime in two-dimensional black phosphorene through acoustic phonon excitation, J. Phys. Chem. Lett. **12**, 3960 (2021).

[26] H. Zhao, E. J. Loren, H. M. van Driel, and A. L. Smirl, Coherence Control of Hall Charge and Spin Currents, Phys. Rev. Lett. **96**, 246601 (2006).

[27] C. Wang, B. Lian, X. Guo, J. Mao, Z. Zhang, D. Zhang, B.-L. Gu, Y. Xu, and W. Duan, Type-II Ising Superconductivity in Two-Dimensional Materials with Spin-Orbit Coupling, Phys. Rev. Lett. **123**, 126402 (2019).

[28] Z. Ji, G. Liu, Z. Addison, W. Liu, P. Yu, H. Gao, Z. Liu, A. M. Rappe, C. L. Kane, E. J. Mele, and R. Agarwal, Spatially dispersive circular photogalvanic effect in a Weyl semimetal, Nat. Mater. **18**, 955 (2019).

[29] J. E. Sipe and A. I. Shkrebtii, Second-order optical response in semiconductors, Phys. Rev. B **61**, 5337 (2000).

[30] B. M. Fregoso, Bulk photovoltaic effects in the presence of a static electric field, Phys. Rev. B **100**, 064301 (2019).

[31] H. Wang and X. Qian, Ferroicity-driven nonlinear photocurrent switching in time-reversal invariant ferroic materials, Sci. Adv. **5**, eaav9743 (2019).

[32] T. Holder, D. Kaplan, and B. Yan, Consequences of time-reversal-symmetry breaking in the light-matter interaction: Berry curvature, quantum metric, and diabatic motion, Phys. Rev. Res. **2**, 033100 (2020).

[33] A. Taghizadeh, F. Hipolito, and T. G. Pedersen, Linear and nonlinear optical response of crystals using length and velocity gauges: Effect of basis truncation, Phys. Rev. B **96**, 195413 (2017).

[34] A. Laturia, M. L. Van de Put, and M. G. Vandenberghe, Dielectric properties of hexagonal boron nitride and transition metal dichalcogenides: From monolayer to bulk, npj 2D Mater. Appl. **2**, 6 (2018).

[35] Z. Jiang, Z. Liu, Y. Li, and W. Duan, Scaling Universality between Band Gap and Exciton Binding Energy of Two-Dimensional Semiconductors, Phys. Rev. Lett. **118**, 266401 (2017).

[36] X. Mu, Y. Pan, and J. Zhou, Pure bulk orbital and spin photocurrent in two-dimensional ferroelectric materials, npj Comput. Mater. **7**, 61 (2021).

[37] R. Fei, L. Z. Tan, and A. M. Rappe, Shift-current bulk photovoltaic effect influenced by quasiparticle and exciton, Phys. Rev. B **101**, 045104 (2020).

[38] P. Zereshki, Y. Wei, F. Ceballos, M. Z. Bellus, S. D. Lane, S. Pan, R. Long, and H. Zhao, Photocarrier dynamics in monolayer phosphorene and bulk black phosphorus, Nanoscale **10**, 11307 (2018).

[39] J. Ahn, G.-Y. Guo, and N. Nagaosa, Low-Frequency Divergence and Quantum Geometry of the Bulk Photovoltaic Effect in Topological Semimetals, Phys. Rev. X **10**, 041041 (2020).

[40] H. Xu, H. Wang, J. Zhou, and J. Li, Pure spin photocurrent in non-centrosymmetric crystals: Bulk spin photovoltaic effect, Nat. Commun. **12**, 4330 (2021).

[41] B. A. Bernevig, T. L. Hughes, and S.-C. Zhang, Orbitronics: The Intrinsic Orbital Current in *p*-Doped Silicon, Phys. Rev. Lett. **95**, 066601 (2005).

[42] R. D. R. Bhat, F. Nastos, A. Najmaie, and J. E. Sipe, Pure Spin Current from One-Photon Absorption of Linearly Polarized Light in Noncentrosymmetric Semiconductors, Phys. Rev. Lett. **94**, 096603 (2005).

[43] R. Fei, X. Lu, and L. Yang, Intrinsic spin photogalvanic effect in nonmagnetic insulator, arXiv:2006.10690.

[44] R. Fei, S. Yu, Y. Lu, L. Zhu, and L. Yang, Switchable enhanced spin photocurrent in Rashba and cubic Dresselhaus ferroelectric semiconductors, Nano Lett. **21**, 2265 (2021).

[45] T. P. Cysne, M. Costa, L. M. Canonico, M. B. Nardelli, R. B. Muniz, and T. G. Rappoport, Disentangling Orbital and Valley Hall Effects in Bilayers of Transition Metal Dichalcogenides, Phys. Rev. Lett. **126**, 056601 (2021).

[46] Y. Pan and J. Zhou, Toggling Valley-Spin Locking and Nonlinear Optical Properties of Single-Element Multiferroic Monolayers Via Light, Phys. Rev. Appl. **14**, 014024 (2020).

[47] B. S. Mendoza, L. Juarez-Reyes, and B. M. Fregoso, Pure spin current injection of single-layer monochalcogenides, arXiv:2012.04604.

[48] T. Barik and J. D. Sau, Nonequilibrium nature of nonlinear optical response: Application to the bulk photovoltaic effect, Phys. Rev. B **101**, 045201 (2020).

[49] H. Wang, C. Zhang, and F. Rana, Surface recombination limited lifetimes of photoexcited carriers in few-layer transition metal dichalcogenide MoS_2, Nano Lett. **15**, 8204 (2015).

[50] I. Niehues, R. Schmidt, M. Drüppel, P. Marauhn, D. Christiansen, M. Selig, G. Berghauser, D. Wigger, R. Schneider, L. Braasch, R. Koch, A. Castellanos-Gomez, T. Kuhn, A. Knorr, E. Malic, M. Rohlfing, S. M. de Vasconcellos, and R. Bratschitsch, Strain control of exciton-phonon coupling in atomically thin semiconductors, Nano Lett. **18**, 1751 (2018).

[51] J. Zhou, H. Xu, Y. Shi, and J. Li, Terahertz driven reversible topological phase transition of monolayer transition metal dichalcogenides, Adv. Sci. **8**, 2003832 (2021).

[52] C. Wang, X. Liu, L. Kang, B.-L. Gu, Y. Xu, and W. Duan, First-principles calculation of nonlinear optical responses by Wannier interpolation, Phys. Rev. B **96**, 115147 (2017).

[53] M. Schlipf and F. Giustino, Dynamic Rashba-Dresselhaus effect, arXiv:2004.10477.

[54] D. Go, F. Freimuth, J.-P. Hanke, F. Xue, O. Gomonay, K.-J. Lee, S. Blügel, P. M. Haney, H.-W. Lee, and Y. Mokrousov, Theory of current-induced angular momentum transfer dynamics in spin-orbit coupled systems, Phys. Rev. Res. **2**, 033401 (2020).

[55] D. Go, D. Jo, C. Kim, and H.-W. Lee, Intrinsic Spin and Orbital Hall Effects from Orbital Texture, Phys. Rev. Lett. **121**, 086602 (2018).

[56] M.-F. Yang and M.-C. Chang, Středa-like formula in the spin Hall effect, Phys. Rev. B **73**, 073304 (2006).

[57] G. Marcelli, G. Panati, and S. Teufel, Theory of conserved spin current and its application to a two-dimensional hole gas, Ann. Henri Poincaré **22**, 1069 (2021).

[58] S. Murakami, Quantum Spin Hall Effect and Enhanced Magnetic Response by Spin-Orbit Coupling, Phys. Rev. Lett. **97**, 236805 (2006).

[59] P. Zhang, Z. Wang, J. Shi, D. Xiao, and Q. Niu, Theory of conserved spin current and its application to a two-dimensional hole gas, Phys. Rev. B **77**, 075304 (2008).

[60] H. Kontani, T. Tanaka, D. S. Hirashima, K. Yamada, and J. Inoue, Giant Intrinsic Spin and Orbital Hall Effects in Sr_2MO_4 ($M = $ Ru, Rh, Mo), Phys. Rev. Lett. **100**, 096601 (2008).

[61] H. Kontani, T. Tanaka, D. S. Hirashima, K. Yamada, and J. Inoue, Giant Orbital Hall Effect in Transition Metals: Origin of Large Spin and Anomalous Hall Effects, Phys. Rev. Lett. **102**, 016601 (2009).

[62] D. Monaco and L. Ulčakar, Spin Hall conductivity in insulators with nonconserved spin, Phys. Rev. B **102**, 125138 (2020).

[63] A. Avdoshkin, V. Kozii, and J. E. Moore, Interactions Remove the Quantization of the Chiral Photocurrent at Weyl Points, Phys. Rev. Lett. **124**, 196603 (2020).

[64] B. I. Sturman, Ballistic and shift currents in the bulk photovoltaic effect theory, Phys. Usp. **63**, 407 (2020).

[65] Z. Dai, A. M. Schankler, L. Gao, L. Z. Tan, and A. M. Rappe, Phonon-Assisted Ballistic Current from First-Principles Calculations, Phys. Rev. Lett. **126**, 177403 (2021).